Peer-reviewed version available at *Materials* **2018**, *11*, 2260; doi:10.3390/ma11112260

Article

Photoactive ZnO Materials for Solar Light Induced Cu_xO-ZnO Catalyst Preparation

Magdalena Brzezińska[1,2], Patricia García-Muñoz[2], Agnieszka M. Ruppert[1], and Nicolas Keller[2,*]

[1] Institute of General and Ecological Chemistry, Faculty of Chemistry, Lodz University of Technology, ul. Żeromskiego 116, 90-924, Łódź, Poland ; agnieszka.ruppert@p.lodz.pl
[2] Institut de Chimie et Procédés pour l'Energie, l'Environnement et la Santé, CNRS/University of Strasbourg, 25 rue Becquerel, 67087 Strasbourg, France ; nkeller@unistra.fr
* Correspondence: nkeller@unistra.fr; Tel.: +33-3-6885-2811

Abstract: In this work, the solar light-induced redox photoactivity of the ZnO semiconductor material was used to prepare at room temperature Cu_xO-ZnO composite catalysts with a control of the chemical state of the copper oxide phase. The preparation of $Cu_2^{(I)}O$-ZnO and $Cu^{(II)}O$-ZnO composite catalysts was achieved by using $Cu(acac)_2$ in THF-water and $Cu(NO_3)_2$ in water as metallic precursor, respectively. Prior to the implementation of the photo-assisted synthesis method, the most efficient photoactive ZnO material was selected among different ZnO materials prepared by the low temperature polyol method and through the precipitation method with carbonates and carbamates as precipitation agent, by taking the photocatalytic degradation of the 4-chlorophenol compound in water under simulated solar light as model reaction. The ZnO support materials were characterized by XRD, BET, TGA, SEM and TEM, and the synthesis method was strongly influencing their photoactivity in terms of 4-chlorophenol degradation and of total organic carbon removal. The most photoactive ZnO material was prepared by precipitation with carbonates and calcined at 300°C, and was taking advantage of a high specific surface area and a small mean crystallite size for achieving a complete 4-chlorophenol mineralization within 70 min of reaction, with a minimum Zn^{2+} released to the solution due to surface photocorrosion. Beside thermal catalysis applications, this work opened a new route for the facile synthesis of Cu_2O-ZnO heterojunction photocatalysts, that could take advantage under solar light of the heterojunction built between the *p*-type semi-conductor Cu_2O with direct visible light band gap and the ZnO semiconductor phase.

Keywords: ZnO; photo-oxidation; 4-chlorophenol; Cu_xO-ZnO catalyst; photodeposition

1. Introduction

Zinc oxide (ZnO) nanostructures are materials with potential applications in many fields of nanotechnology, due to the large variety of nanometric structures or architectures that can be synthesized [1]. Beside numerous applications in

optoelectronics, electronics, laser technology, converters and energy generators or as gas sensors [1-6] , zinc oxide (ZnO) nanostructures have received special attention for being used directly as (photo)catalyst or as catalyst support.

Indeed, ZnO is a II–VI compound semi-conductor that has emerged as a promising candidate as heterogeneous photocatalyst under near-UV irradiation in environmental applications such as the removal of a large range of organic and inorganic contaminants from environmental water and wastewater, including some of the most toxic and refractory molecules in water like pesticides, herbicides, and dyes [7]. It is characterized by a direct wide band gap close to that of anatase TiO_2 (3.2–3.37 eV), a suitable location of both conduction and valence bands, strong oxidation ability, low cost, abundance and a large exciton binding energy of 60 meV at room temperature [1,8-11] so that exciton emission processes can persist at or even above the room temperature. It has already been reported that the electron lifetime can be significantly higher and that the rate of recombination can be lower in ZnO in comparison to TiO_2, making it an attractive material worth to investigate for photocatalytic applications [12]. Further, the photocatalytic activity of ZnO can be enhanced by designing ZnO supported metal nanoparticle photocatalysts, with promising results mainly in the case [13] of Au and Ag [14-19]. In such hybrid metal/ZnO nanostructure, the supported nanoparticles are proposed i) to act as a sink for photoinduced electrons, so that the metal/semi-conductor interface could promote effective charge separation with efficient interfacial charge transfer, or ii) to induce plasmonic effects either through the direct injection of hot (excited) electrons from the metal to the conduction band of ZnO thanks to intimate electrochemical contact between the plasmonic particle and the semiconductor, or through an near-field enhancement mechanism with overlap between the plasmon wavelength and the photocatalyst absorption.

ZnO nanostructures are also widely investigated as catalyst support in several reactions of high fundamental or applicative interest, such as the methanol oxidation [20], the low-temperature methanol synthesis [21,22], the production of hydrogen from methanol by steam reforming, partial oxidation, or a combination thereof [23], the steam reforming of ethanol, the glycerol hydrogenolysis [24], various transesterification reactions [25], or selective hydrogenation reactions [26-30]. The active metals or metal oxides mainly included Cu, Pd, Au, Ag, Co, Ni, Rh, Ir and Pt and were usually stabilized on the ZnO support *via* incipient wetness or wet impregnation, ion exchange or (co)-precipitation [31].

The high interest of using zinc oxide as a support result from to its valuable physico-chemical properties. Hydrogenations reactions can take benefit from strong metal-support interactions and from the formation of alloys with the supported metals in reductive atmosphere. This behavior is responsible for the modification of the electronic properties of the supported active metals, which in turn results in significant activity and selectivity enhancements in many catalytic reactions. Activity improvement can be also associated with the existence of a hydrogen spillover phenomena taking place in the case of zinc oxide supported metal catalysts.

The most widely used methods for preparing supported metal catalysts combine the implementation of consecutive elemental operations, with first the introduction of the metal precursor onto the support. The reduction treatment usually consists in a thermal treatment with external hydrogen, or in a chemical reduction in solution with reducing agents such as sodium borohydrate or hydrazine. Depending on the method, the supported catalysts can suffer from heterogeneous metal particle size distributions, from detrimental temperature-activated side-reactions between the metal precursor and the support and from limitations in terms of metal loadings.

It has been demonstrated that the synthesis method is playing a key role in the preparation of ZnO materials with varied bulk and surface physico-chemical properties, and many chemical methods have been reported for synthesizing ZnO nanostructures, including notably mechanico-chemical processes, precipitation, sol-gel, solvothermal and hydro-thermal method, methods using an emulsion or microemulsion environment, sonochemical or microwave-based methods [4-6, 11].

Therefore, the aim of the article is double. First, it aims at selecting an appropriate preparation method for synthesizing photoactive ZnO under solar light. This was achieved by studying the influence of the synthesis method on the ZnO photoactivity, taking the photocatalytic degradation of 4-chlorophenol in water under solar light as model reaction. Further, the solar light-induced redox photoactivity developed by ZnO was used to prepare at room temperature Cu_xO-ZnO catalysts with Cu chemical state control, that are of interest in fundamental and applicative reactions, and that do not require the use of any thermal treatment, or of any gaseous or liquid reductant for controlling the Cu chemical state.

2. Materials and Methods

2.1 Synthesis of ZnO materials

2.1.1. Polyol method

In the polyol synthesis, 1.5 g of zinc (II) acetate dihydrate ($Zn(OAc)_2.2H_2O$ Sigma-Aldrich, ACS reagent, ≥98%) was introduced into 50 ml of propane-1,3-diol solvent ($C_3H_8O_2$, Sigma-Aldrich, 98%). The obtained mixture was kept under continuous stirring and under reflux at 160°C for 15 min or 60 min. Afterwards, the precipitate obtained was cooled down, centrifuged for 20 min at 3500 rpm, and finally washed and filtrated under vacuum several times with absolute ethanol (Sigma-Aldrich). The synthesized powder was dried at 100°C for 12 h. The samples obtained were labelled as ZnO-P-15 and ZnO-P-60 according to the reflux duration.

2.1.2. Precipitation with Na_2CO_3

In this precipitation synthesis method, 1.75 g of zinc (II) acetate dihydrate and 0.84 g of sodium carbonate (Na_2CO_3, Sigma-Aldrich, 99.5%) were dissolved under stirring in 50 ml of distilled water, respectively. Both aqueous solutions were mixed, and the obtained precipitate was aged at room temperature in the mother liquor for 24 h under continuous stirring. The suspension was further centrifuged for 30 min at 3500 rpm, and finally washed and filtrated under vacuum with distilled water. The resulting powder was dried at 100°C for 12 h and subsequently calcined at a temperature of 300°C to 500°C for 2 h with a 10°C/min heating rate, leading to the ZnO-C material series.

2.1.3. Precipitation with $NH_2CO_2NH_4$

Analogous to the previous synthesis, 10.98 g of zinc (II) acetate dihydrate and 4.29 g of ammonium carbamate ($NH_2CO_2NH_4$, Sigma Aldrich, 99%) were dissolved under stirring in 50 ml of distilled water respectively. Both aqueous solutions were mixed, and obtained precipitate was aged at room temperature in the mother liquor for 30 min under continuous stirring. The suspension was further centrifuged for 30 min at 3500 rpm, and finally washed and filtrated under vacuum with distilled water. The resulting powder was dried at 100°C for 12 h and subsequently calcined at a temperature of 400°C to 500°C for 2 h with a 10°C/min heating rate, leading *eg.* to to the ZnO-c material series.

2.2 Photoassisted preparation of Cu-ZnO catalysts

The photoassisted preparation of Cu-ZnO catalysts was performed by irradiating with solar light a suspension of the ZnO semi-conductor support containing $Cu(acac)_2$ or $Cu(NO_3)_2$ as metallic precursors. The irradiation was provided by an Atlas Suntest XLS+ reaction chamber equipped with a Xenon arc lamp adjusted to a 500 W/m² irradiance (with a 30 W/m² UV-A content) and a Solar ID 65 filter for simulating the solar exposition according to ICH Q1B guidelines (320-800 nm wavelength range). The amount of copper precursor used was adjusted to target a Cu content of 10 wt.% on the ZnO support.

2.2.1. $Cu(acac)_2$ in THF-H_2O solvent

Dissolution of 20.8 mg of copper(II) acetylacetonate (Sigma-Aldrich, 97%) has been achieved for 30 min at 60°C under stirring in THF (Sigma-Aldrich, 99%) - water mixture with a 2:9 (v/v) ratio, before 45 mg of the ZnO support was dispersed under stirring in 100 mL of copper solution in a beaker-type glass reactor at a 0.21 g/L concentration. Prior to irradiation, the suspension was stirred in the dark for 0.5 h at 60°C to ensure the establishment of the adsorption/desorption equilibrium, before the photoassisted synthesis was performed under stirring at 60°C under solar light. The synthesis was monitored by UV-vis spectrophotometry by following the disappearance of the absorption peak at λ =245 nm. The samples were washed and filtrated under vacuum several times with distilled water, and finally dried at 100°C for 1 h [13].

2.2.2. $Cu(NO_3)_2$ in H_2O solvent

The protocol was similar to that followed with $Cu(acac)_2$. In this case, dissolution of 38 mg of copper(II) nitrate trihydrate (Sigma-Aldrich, p.a) was performed in water at room temperature, before 90 mg of ZnO was dispersed under stirring in 100 mL of copper solution in a beaker-type glass reactor at a 0.38g/L concentration. Prior to irradiation, the suspension was stirred in the dark for 30 min at 60°C to ensure the establishment of the adsorption/desorption equilibrium, before the photoassisted synthesis was performed under stirring under solar light for 2 h. The synthesis was monitored by UV-vis spectrophotometry by following the disappearance of the absorption peaks at λ = 800 nm. The samples were washed and filtrated under vacuum several times with distilled water, and finally dried at 100°C for 1 h.

2.3. Characterisation techniques

The crystallographic structure of the powders has been characterized by X-ray diffraction patterns (XRD) recorded on a D8 Advance Bruker diffractometer in a θ/θ mode and using the $K_{\alpha 1}$ radiation of a Cu anticathode (λ = 1.5406 Å).

The surface area measurements have been carried out on a Micrometrics Tristar 3000 using N_2 as adsorbent at −196 °C with a prior outgassing at 100°C overnight in order to desorb the impurities or moisture. The Brunauer–Emmett–Teller (BET) specific surface area has been calculated from the N_2 adsorption isotherm.

Scanning electron microscopy (SEM) was performed in secondary electron mode on a JEOL JSM-6700 F FEG microscope.

Transmission electron microscopy (TEM) was performed using a JEOL 2100F with a point resolution of 0.2 nm. The interplanar spacings were calculated using ImageJ software.

Thermogravimetric analysis (TGA) was carried out with a 20% (v/v) O_2/N_2 mixture at a flow rate of 40 mL/min at a heating rate of 10°C/min from 25°C to 600°C using a Q 5000 TA Instrument thermoanalyzer.

The copper content in the catalysts were determined by chemical analysis after a microwave-assisted acidic dissolution in aqua regia at 185°C under autogenic pressure. Inductively coupled plasma optical emission spectroscopy (ICP-OES) was carried out on an Optima 7000 DV spectrometer (Perkin Elmer) at the Analysis Plateform of IPHC-Strasbourg, France.

2.4 Evaluation of the photocatalytic efficiency

The experiments were carried out in an Atlas Suntest XLS+ reaction chamber equipped with a Xenon arc lamp of 1700 W adjustable power. The equipment has a Solar ID 65 filter to limit the UV radiation at 320 nm, simulating solar exposition according to ICH Q1B guidelines. The runs were performed adjusting the lamp

power to 500 W/m² with a simulated solar emission within 300–800 nm. The reaction volume was 500 mL and the starting concentration of 4 Cl-phenol 25 mg L^{-1}, corresponding to a carbon load of 14.8 ppm. The ZnO catalyst load was 1 g L^{-1}. At each time interval, 20 mL of solution has been sampled and then filtered through 0.20 µm porosity filter to remove the photocatalyst powder if any, before the concentration of 4-chlorophenol has been determined by UV-Visible spectrophotometry (Cary 100 scan) by monitoring the disappearance of the main absorption peak at λ = 224 nm, and Total Organic Carbon measurements were performed using a Shimadzu TOC-L analyzer to determine the organic carbon load.

A procedure was established for photocatalytically cleaning the ZnO materials under UV-A or solar light prior the chlorophenol removal, consisting in the continuous stirring of the as-synthesized ZnO catalyst in ultrapure Milli-Q water under either simulated solar light for 2 h or UV-A light for 16 h. UV-A light was provided by blacklight lamps (Philips PL-L 24W/10/4P) emitting at 365 nm with an irradiance of 60 W/m²), while the UV-A fraction of the simulated solar light corresponded to a 30 W/m² irradiance, as measured using a wide-band RPS900-W rapid portable spectroradiometer from International Light Technology.

3. Results

3.1. Characterization of ZnO materials

The main physico-chemical properties of the ZnO are reported in Table 1. Figure 1A and 1B shows the XRD patterns of the dried ZnO precursors and of the final ZnO materials synthesized *via* the polyol and the precipitation routes.

In the case of the polyol method, the XRD pattern shown in Figure 1a displayed the diffraction peaks corresponding to ZnO crystallized in the hexagonal wurtzite structure and attributed to the diffraction of the (100), (002), (101), (102), (110), and (103) planes for the most intense characteristic peaks (space group P63mc, JCPDS No. 00-036-1451) [5, 14-16]. As reported for the polyol synthesis, the ZnO material had a good crystallinity without any post-synthesis calcination treatment.

By contrast, the dried material obtained in the case of both precipitation methods consisted in a $Zn_5(CO_3)_2(OH)_6$ zinc carbonate hydroxide, or hydrozincite phase, in the monoclinic structure [17] with the diffraction of the (111), (310), (100), (311), (220) and (021) planes for the most intense characteristic peaks (JCPDS 19-1458). Han et al. [18] have proposed that the reactions during the formation of $Zn_5(CO_3)_2(OH)_6$ are likely as follows:

$$Zn(CH_3COO)_2 \rightarrow Zn^{2+} + 2[CH_3COO]^- \quad (1)$$

$$(CH_2)_6N_4 + 10H_2O \rightarrow 6HCHO + 4OH^- + 4[NH_4]^+ \quad (2)$$

$$HCHO + O_2 + 2OH^- \rightarrow CO_3^{2-} + 2H_2O \quad (3)$$

$$5Zn^{2+} + 2CO_3^{2-} + 6OH^- \rightarrow Zn_2(CO_3)_2(OH)_6 \quad (4)$$

The zinc carbonate hydroxide phase being thermally stable below 200°C, its decomposition into ZnO was evidenced by XRD characterization and TGA analysis in Figure 1b and Figure 2, respectively. After calcination of the zinc carbonate hydroxide at a temperature higher than 300°C, the XRD pattern exhibited the diffraction peaks corresponding to hexagonal ZnO, while, according to the weight loss of 28% ± 1% observed in TGA, the decomposition process can be described as follows, corresponding to a theoretical weight loss of 28,4%:

$$Zn_2(CO_3)_2(OH)_6 \rightarrow 5ZnO + 2CO_2 + 3H_2O \quad (5)$$

The absence of any weight loss during the TGA of the calcined ZnO materials confirmed the efficiency of the thermal decomposition process. By contrast, a very small weight loss of 6% was observed on the ZnO prepared *via* the polyol method, suggesting the residual presence of propane 1-3 diol solvent or acetate species [19].

In agreement with the previous works of Fkiri et al. [14], the ZnO materials synthesized *via* the polyol method displayed a good crystallinity without any post-synthesis heat treatment, and exhibited the smallest average crystallite size at 7 nm and 11 nm, for an aging duration of 15 min and 60 min, respectively. The ZnO materials prepared *via* both precipitation routes had a larger mean crystallite size, as a result of the necessary calcination treatment at temperatures ranging from 300°C to 500°C, the use of carbonates as precipitating agent allowing to maintain a smaller mean crystallite size in the 10-20 nm range, while it strongly increased to 28-30 nm in the case of the carbamate agent. For a similar calcination temperature, ZnO prepared with carbamates displayed a larger crystallite size than its carbonate counterpart, *eg*. 28 nm *vs*. 20 nm at a temperature of 400°C.

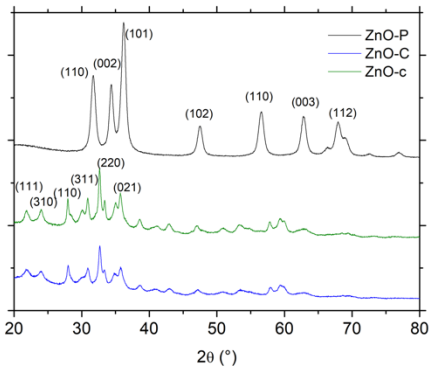

(**a**)

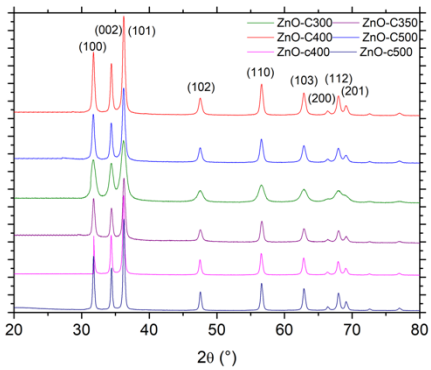

(**b**)

Figure 1. XRD of (a) the dried materials and (b) the calcined materials.

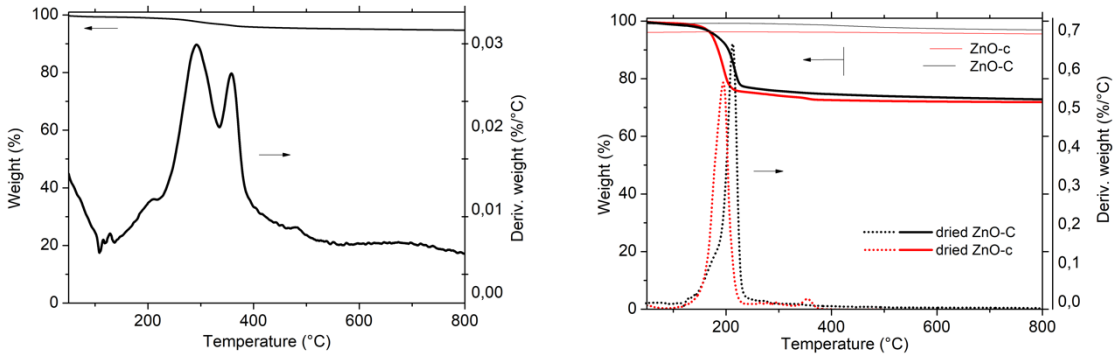

(**a**) (**b**)

Figure 2. TGA of the materials after the drying step synthesized by (a) the polyol method, (b) the carbonate-derived precipitation method and the carbamate-derived precipitation method. The weight loss observed on the ZnO-C and ZnO-c materials after calcination at 300°C and 400°C, respectively, was reported.

Table 1. Main physico-chemical properties of ZnO materials.

Sample	Mean crystallite size (nm)[a]	BET surface area (m^2/g)[b]	Pore volume (cm^3/g)	Average pore diameter (nm)
ZnO-P-15	7	78	0.13	5
ZnO-P-60	11	66	0.09	6
ZnO-C-300	10	68	0.45	21
ZnO-C-350	22	41	0.24	21
ZnO-C-400	20	29	0.21	27
ZnO-C-500	18	29	0.24	30
ZnO-c-400	28	12	0.10	30
ZnO-c-500	30	6	0.05	28

[a] derived from XRD pattern, as the average size of the coherent diffraction domains, calculated from the Scherrer equation applied with the usual assumption of spherical crystallites. It was estimated from the full-width at half-maximum (FWHM) of the diffraction peaks of ZnO (102), (110), and (103) planes.

Figure 3a shows N_2 adsorption–desorption isotherms of ZnO materials. The ZnO-P materials displayed type IV isotherms, corresponding to mainly

mesoporous solids with a mainly H2-type hysteresis characteristic of interconnected mesopores with non-uniform shape or size [14]. For ZnO obtained by precipitation, the isotherms turned to be preferentially of type II with H3-type hysteresis, what suggested that the porosity mainly resulted from macropores (or large mesopores) and was characteristic of aggregates or agglomerates of nanoparticles forming slit shaped pores with non-uniform size and/or shape. This was in agreement with the corresponding pore size distributions shown in Figure 3b, that evidenced clearly the influence of the synthesis method on the average pore size.

The specific surface areas of the ZnO materials were ranging from 6 m^2/g to 78 m^2/g without any microporous contribution. Among the different materials, the ZnO-P and ZnO-C-300 samples had the highest specific surface areas, within the 66-78 m^2/g range, in agreement with their smallest mean crystallite sizes of 7-11 nm. The increase in the calcination temperature of carbonate-derived ZnO materials from 300°C to 500°C led to a progressive decrease in the surface area from 68 m^2/g to 29 m^2/g, as a result of the slight increase in mean crystallite size. It is worth noting that the carbamate-derived ZnO samples calcined at 400°C and 500°C displayed a lower surface area than their carbonate-derived counterparts, at 12 m^2/g and 6 m^2/g respectively, in agreement with a larger mean crystallite size.

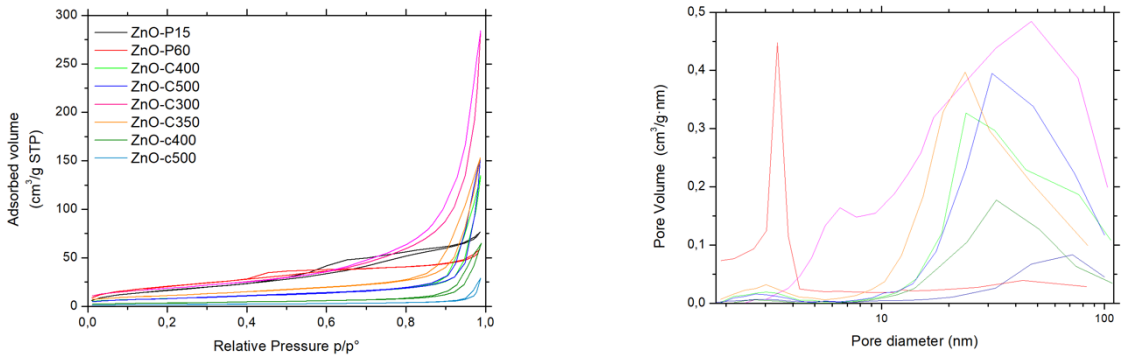

(**a**) (**b**)

Figure 3. (a) N_2 adsorption-desorption isotherms and (b) pore size distributions of ZnO materials.

The synthesis method had no influence on the gand gap of the ZnO materials, graphically estimated at 3.2 eV *via* Tauc plot derived from UV–vis diffuse reflectance analysis, in agreement with the literature (not shown) [14,32]. Therefore, the ZnO materials will be activated by incident photons with wavelengths within the UV-A range, whether the photocatalytic tests are performed under solar light or pure UV-A light.

Figure 4 depicts a selection of SEM images of the different ZnO materials and evidence that both the synthesis method and the nature of the precipitating agent strongly influenced the morphology of the ZnO material. ZnO from polyol synthesis consisted in large spherical shape aggregates (100-200 nm) of small-size ZnO nanoparticles with a mean crystallite size around 10 nm, in agreement with the that derived from the XRD patterns. The interplanar spacing of 0.26 nm shown in Figure 5 was consistent with the (002) plane of hexagonal (wurtzite) ZnO crystallites confirmed the nature.

Peer-reviewed version available at *Materials* **2018**, *11*, 2260; doi:10.3390/ma11112260

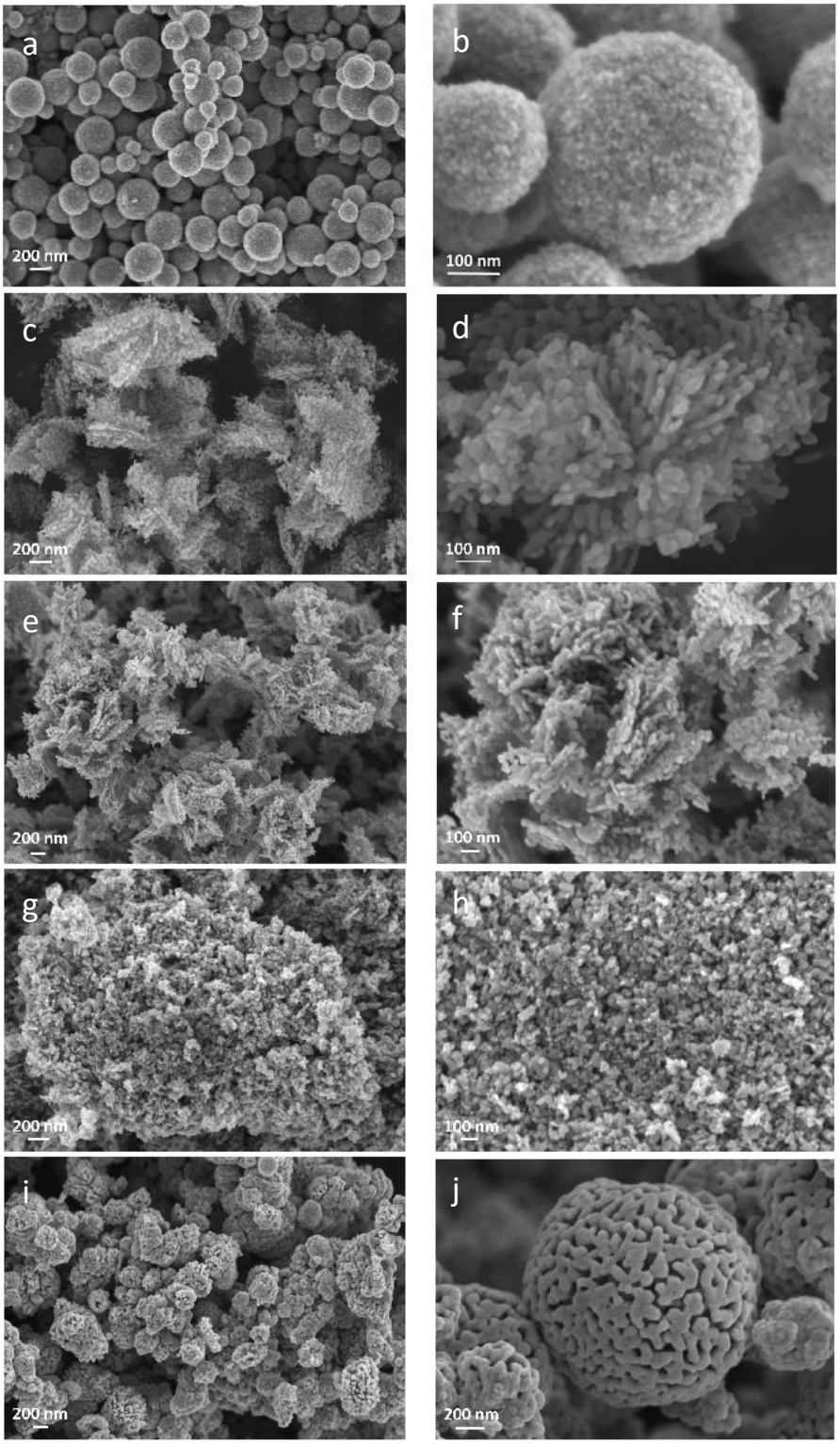

Figure 4. SEM of ZnO materials synthesized through the polyol method (a,b), the precipitation with carbonates at 300 °C (c,d), 400 °C (e,f), 500 °C (g,h) and the precipitation with carbamates at 400°C (i) and 500°C (j).

TEM images of ZnO synthesized *via* the different methods are shown in Figure 5. Whatever the synthesis method, they evidenced interplanar spacings of 0.28 nm and 0.25 nm consistent with the (100) and (101) planes of the hexagonal wurtzite ZnO phase [JCPDS No. 00-036-1451] and confirmed the general morphology of the

Peer-reviewed version available at Materials 2018, 11, 2260; doi:10.3390/ma11112260

wurzite ZnO materials previously observed in SEM images, with crystallite sizes in agreement with those derived from the XRD patterns.

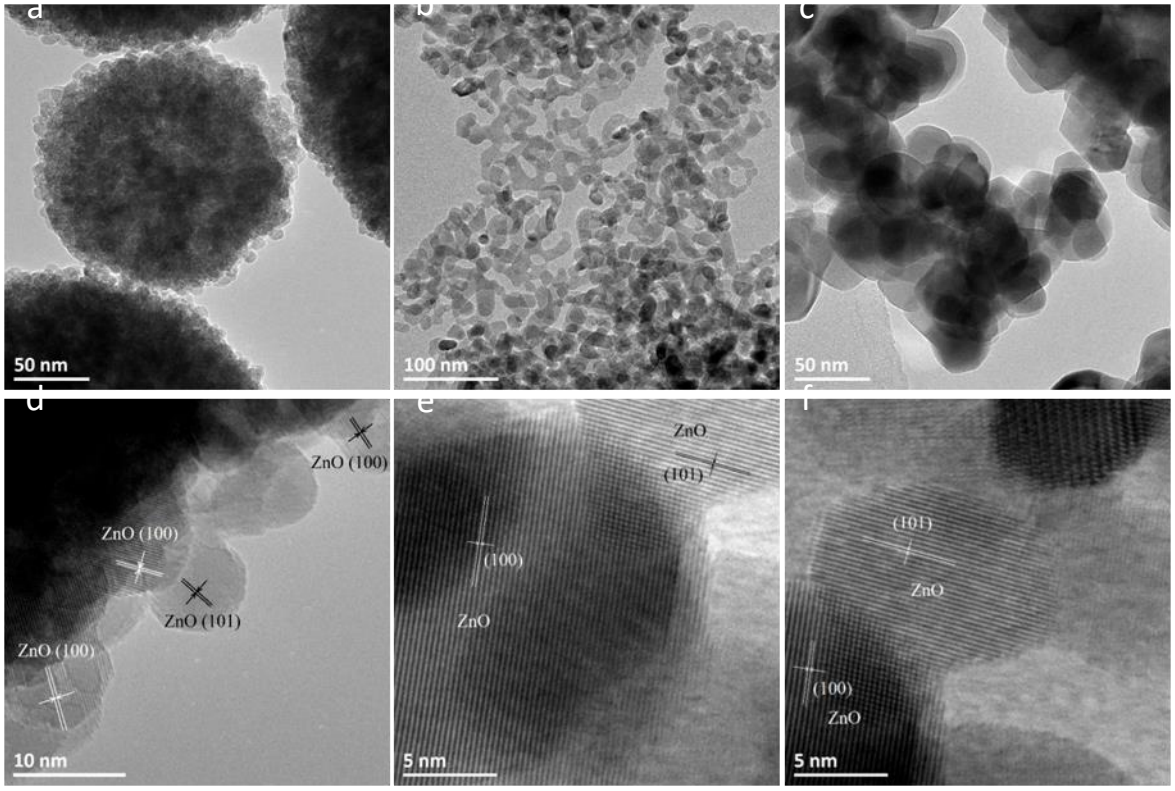

Figure 5. TEM images of ZnO materials synthesized through (a,d) the polyol method, (b,e) the precipitation with carbonates and (c,f) the precipitation with carbamates, evidencing the general morphology of the materials and interplanar spacings of 0.24 nm and 0.25 nm consistent with the (100) and (101) planes of hexagonal wurtzite ZnO crystallites.

3.2. Photocatalytic activity of ZnO

3.2.1. Influence of a photocatalytic pre-cleaning step

The photocatalytic activity of the as-synthesized ZnO materials was first evaluated in water under solar light using 4-Cl-phenol as test molecule, and two catalysts prepared *via* the polyol method and the carbonate-through precipitation method were selected for studying the influence of a photocatalytic pre-cleaning step, *ie.* the dried ZnO-P-15 and calcined ZnO-C-300 samples, respectively (Figure 6).

First, no detectable degradation of chlorophenol has been observed for 3 h under simulated solar light, indicating that the chlorophenol photolysis can be neglected in the experimental conditions, as reported by Eslami et al. and Gaya et al. [33,34].

As depicted in Figure 6a, the pollutant evolution along time under irradiation showed that both ZnO catalysts were able to oxidize the phenolic compound until its complete degradation, achieved within 90 min and 150 min of reaction on the ZnO-P-15 and ZnO-C-300 materials. By contrast, a TOC release to the aqueous

solution was evidenced during the establishment of the adsorption/desorption equilibrium in the dark for both uncleaned ZnO catalysts before TOC removal was observed with a kinetic rate constant k'_{TOC} of 0.13 ppm/min and 0.18 ppm/min for ZnO-P-15 and ZnO-C-300 catalysts, respectively (Figure 6b). This TOC release was notably very pronounced in the case of ZnO synthesized *via* the polyol route, for which no thermal treatment was applied, with a TOC overshoot of 15 ppm at the beginning of the reaction, while only 4 ppm of extra TOC was released with the ZnO-C-300 catalyst. This TOC release difference was in agreement with the TGA analyses.

The catalyst behavior was strongly affected by applying a photocatalytic cleaning step prior the chlorophenol removal, that consisted in the continuous stirring of the as-synthesized ZnO catalyst in ultrapure Milli-Q water under either simulated solar light (2 h, 25 W/m^2 UV-A irradiance) or UV-A (16 h, 60 W/m^2 irradiance). Figure 6c shows in the case of UV-A that those carboned species can be mineralized during the photocatalytic pre-cleaning step of the as-synthesized materials, and the volcano-like TOC profile observed was attributed to the release and subsequent mineralization of carbon-containing residues coming from the precursors used in the ZnO syntheses remaining adsorbed at the catalyst surface or trapped in the bulk of the ZnO crystallites. It confirmed that ZnO synthesized *via* the polyol method contained larger amounts of carboned residues than its counterparts obtained *via* the precipitation approach. They were potentially blocking the ZnO active sites and thus being in competition with the chlorophenol pollutant for the oxidative species, or acting as recombination centers in the ZnO crystallite bulk for the photogenerated charge carriers.

(a)

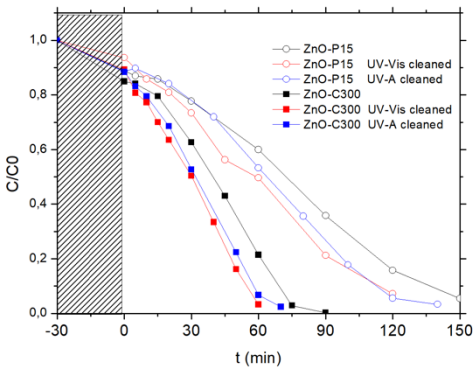

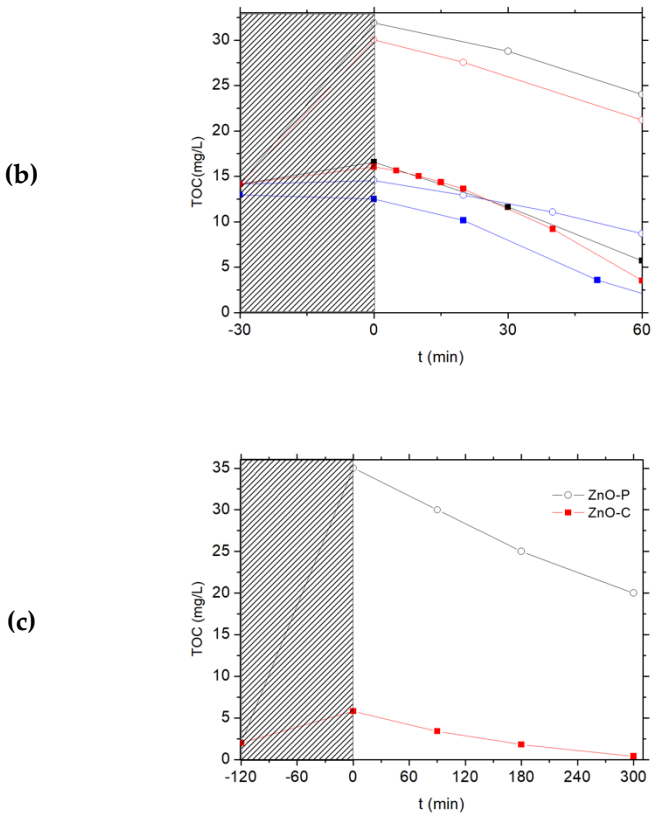

Figure 6. Influence of the photocatalytic pre-cleaning step on (a) the 4-Ch-phenol and (b) the TOC concentration evolution upon photocatalysis with ZnO materials. (C) Evolution of the TOC concentration along the photocatalytic pre-cleaning step of the as-synthesized ZnO-P and ZnO-C materials under UV-A light in ultrapure Milli-Q water.

Performing the cleaning procedure under solar light or UV-A light allowed the degradation rates obtained with the ZnO materials to be improved, as it can be observed in Figures 6a and 6b. Both ZnO catalysts cleaned under solar light or UV-A displayed a faster disappearance of chlorophenol than their uncleaned counterparts. It should be noted that performing the pre-cleaning step for 2 h with a 25 W/m^2 UV-A irradiance (*ie.* solar light as incident light) allowed already a significant enhancement of the kinetic rate constant for the chlorophenol degradation to be obtained, while by contrast the initial TOC release was only slightly improved. The TOC overshoot was totally suppressed only when the pre-cleaning step was performed under UV-A light for 16 h (60 W/m^2 irradiance).

3.2.2. Photocatalytic activity of ZnO materials

Figure 7 shows the evolution with time under irradiation of the 4-Cl-Phenol and TOC concentrations observed on the different ZnO catalysts after the photocatalytic cleaning step under UV-A light has been applied for 2 h. Table 2 shows the corresponding kinetic rate constants of 4-Cl-Phenol and TOC removal.

Peer-reviewed version available at *Materials* **2018**, *11*, 2260; doi:10.3390/ma11112260

Whatever the cleaned material tested, no significant TOC release was observed at the beginning of the test, confirming the efficiency of the photocatalytic pre-cleaning step. Globally, the ZnO-C materials prepared by precipitation with carbonates displayed the highest activity for both the removal of 4 Cl-phenol and that of TOC when compared to their counterparts prepared *via* the polyol method of using the carbamates as precipitation agent. Among the carbonate-through precipitation ZnO series, the highest kinetic rate constants of k'_{Phenol} = 0.21 mg/L/min and k'_{TOC} = 0.18 mg/L/min were obtained with the ZnO-C-300 catalyst, for which the complete mineralization of the pollutant has been achieved within 70 min of irradiation. This activity fairly improves the results found in literature for 4-chloro-phenol removal with ZnO catalyst under UVA irradiation [20]. Gaya et al. reached the complete 4-Cl-Phenol depletion in 3 h using 2 g/L of ZnO.

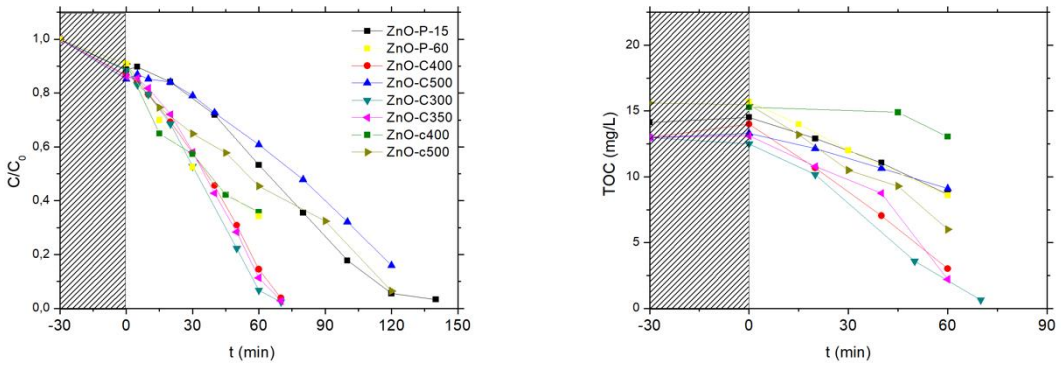

(**a**) (**b**)

Figure 7. 4-Cl-Phenol concentration (a) and TOC concentration (b) evolution upon photocatalysis with UV-A light cleaned ZnO materials.

ZnO obtained by the polyol and carbamate precipitation methods exhibited reduced kinetic constant rate for phenol disappearance and TOC removal, in some cases even two orders of magnitude smaller than for the most active ZnO sample. Further, among the ZnO materials prepared with carbonates, ZnO calcined at the highest temperature of 500°C displayed significantly lower activity compared to that shown by its counterparts calcined in the 300-400°C range.

We may propose that the ZnO-C-300 photocatalyst takes advantage from a higher specific surface area as well as from a large pore volume and a large mean pore size, that facilitate the access of the 4-chlorophenol reactant and of the reaction intermediates to the ZnO surface sites. By contrast, the high surface area ZnO obtained by the polyol method probably suffered from a very low pore volume and mean pore size, while the low surface area of the ZnO-c prepared with carbamate was assumed to be detrimental to the removal efficiency.

Table 2. Pseudo first-order kinetic rate constant of 4-Cl-Phenol removal and zero order rate constant of TOC removal obtained on UV-A light cleaned ZnO catalysts (with the corresponding linear regression coefficients)

Catalyst	k '$_{TOC}$ (mg/Lmin)/R^2	k'$_{Phenol}$ (mg/Lmin)/R^2
ZnO-P15	0.097/0.99	0.008/0.98
ZnO-P60	0.130/0.88	0.011/0.94
ZnO-C300	0.180/0.99	0.210/0.99
ZnO-C350	0.173/0.90	0.017/0.99
ZnO-C400	0.180/0.99	0.014/0.99
ZnO-C500	0.071/0.99	0.007/0.97
ZnO-c400	0.030/0.89	0.010/0.93
ZnO-c500	0.153/0.98	0.007/0.98

As far as ZnO is concerned, surface photocorrosion remains one of its main drawbacks for being used as in water treatment. Photocorrosion consists in the dissolution of the ZnO surface with release of Zn^{2+} to the reaction media, so that the catalyst suffers from deactivation with time under irradiation as well as from intrinsic limitation in terms of reusability. The surface corrosion of ZnO is considered to be induced by photogenerated h^+ and the overall reaction of the ZnO surface dissolution can be expressed as follow:

$$ZnO + 2h^+ \rightarrow Zn^{2+}_{aqueous} + 0.5O_2 \quad (6)$$

According to previous works, the overall surface photocorrosion process consists in two low-rate steps followed by two high-rate steps as follows [35,36] :

$$O^{2-}_{Surface} + h^+ \rightarrow O^-_{Surface} \quad (7)$$

$$O^-_{Surface} + 3O^{2-} + 3h^+ \rightarrow 2(O - O^{2-}) \quad (8)$$

$$(O - O^{2-}) + 2h^+ \rightarrow O_2 \quad (9)$$

$$2Zn^{2+} \rightarrow 2Zn^{2+}_{aqueous} \quad (10)$$

Therefore, it was of high interest to evaluate the influence of the synthesis method on the stability of the ZnO photocatalysts in terms of Zn^{2+} release to the media, expressed as the percentage of Zn^{2+} released from the ZnO catalysts into the water (Figure 8). In a first approximation, the materials with a higher activity exhibited in

Preprints (www.preprints.org) | NOT PEER-REVIEWED | Posted: 22 September 2018 doi:10.20944/preprints201809.0447.v1

Peer-reviewed version available at Materials 2018, 11, 2260; doi:10.3390/ma11112260

a higher stability, with a lower release of Zn^{2+} cation to the solution being observed for the most active catalysts and globally a lower release for ZnO material series prepared by precipitation with carbonates, *eg.* a 0,016 fraction in the case of the most active catalyst ZnO-C-300.

The ZnO-C-500 material displayed a better stability than its counterparts calcined at 300°C, but was suffering from a largely lower activity under UV-A light. Therefore, based on the kinetic rate constants derived from both the chlorophenol disappearance and the TOC evolution curves, as well as on the level of Zn^{2+} release to the media, this fast screening allowed the ZnO-C-300 material obtained *via* the precipitation method with carbonates and calcined at 300°C to be selected for implementing subsequently the solar light photo-assisted preparation of the Cu-ZnO hybrid catalysts in the next section.

However, we would like to point out that the surface photocorrosion of ZnO materials remained a key-issue for using such a material as photocatalyst in water treatment. Indeed, a strong loss of activity was observed when performing sequential runs on the ZnO-C-300 photocatalyst. Using the TOC conversion achieved after 75 min of test as indicator (*ie.* the duration necessary for achieving full TOC conversion in the run#1), Table 3 evidences that the surface photocorrosion was accompanied by an important loss of activity with sequential runs.

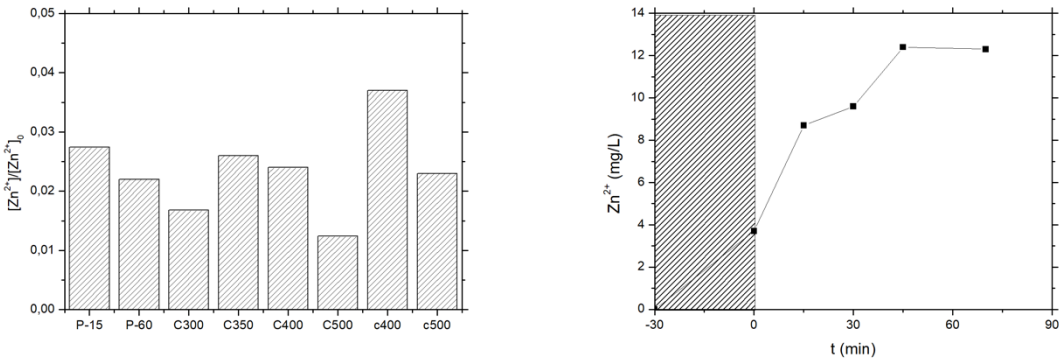

(**a**) (**b**)

Figure 8. Fraction of Zn^{2+} released into the water (a) at the end of the photocatalytic run with ZnO materials and (b) as a function of time under irradiation in the case of the ZnO-C-400 catalyst.

Table 3.TOC conversion after several sequential photocatalytic runs with the ZnO-C300 catalyst.

Run	X_{TOC}(%)
First	100
Second	88

Third	61

3.3. Preparation of Cu-ZnO catalysts by photoassisted synthesis method

The photoassisted preparation of Cu-ZnO catalysts was implemented using the ZnO-C-300 material as semi-conductor support, since the first part of this work evidenced that it displayed the highest photoactivity in terms of removal of both chlorophenol and TOC, as well as a high photo-stability in water. Both $Cu(acac)_2$ and $Cu(NO_3)_2$ metallic precursors were used. Figure 9 depicts the disappearance curves of both $Cu(acac)_2$ and $Cu(NO_3)_2$ metallic precursors during the photon-assisted synthesis in the presence of the ZnO-C-300 catalyst, derived from the evolution of the UV-vis absorbance spectra as a function of the illumination time.

First, photolysis of the copper precursors could be neglected under solar light in our experimental conditions, since no changes of the UV-vis spectra was observed whatever the precursor used (not shown). The evolution with time of the C/C_0 relative concentrations evidenced that the photodeposition occured on the ZnO support, and further that the copper precursor nature influenced the kinetics of the photodeposition process at the surface of the irradiated ZnO support. However, it has to be noticed that the time-monitoring of the photo-deposition process was more difficult using the nitrate precursor than its acetylacetonate counterpart. Indeed, the ability of semi-conductor photocatalysis to perform nitrate reduction and nitrate oxidation in water led to produce first nitrite as initial intermediate (very unstable and easily oxidized back to nitrate) and further higher oxidation state products such as ammonia. The UV-vis signature of those N-compounds is known to overlap around similar absorption wavelengths, so that the photodeposition was monitored in a first approximation by following the disappearance of the low intensity absorption peak at λ = 800 nm related to the Cu^{2+} concentration, which resulted in a less accurate time-monitoring. However, ICP-OES analysis revealed that the Cu-ZnO catalyst had a Cu content of 9.7 wt.%, in good agreement with the targeted theoretical amount of 10 wt.%. By contrast, only a Cu content of 7 wt.% was obtained in the case of the $Cu(acac)_2$ precursor. This difference was attributed to a possible release of non-steadily anchored Cu species during the washing of the Cu-ZnO materials directly after the photoassisted synthesis.

Peer-reviewed version available at Materials 2018, 11, 2260; doi:10.3390/ma11112260

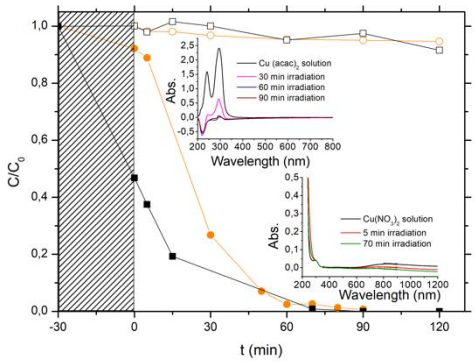

Figure 9. Disappearance curves of (□) the $Cu(NO_3)_2$ and (●) the $Cu(acac)_2$ precursors during the photon-assisted synthesis in the presence of the ZnO-C-300 catalyst. Blank photolysis experiments in the absence of ZnO photocatalyst for (□□) $Cu(NO_3)_2$ and (◦) $Cu(acac)_2$ precursors. Insert: UV-vis absorbance spectra evolution as a function of the illumination time for both precursors (selected analysis times are reported for not overloading the UV-vis absorbance graphs).

3.4. Crystallographic and morphological characterization of Cu-ZnO catalysts

Figure 10 show the XRD patterns of both Cu-ZnO catalysts. In the case of the $Cu(acac)_2$ precursor, besides the diffraction peaks of ZnO crystallized in the hexagonal wurtzite structure, additional diffraction peaks have been observed at 29.6°, 42.2°, 61.3° and 73.4°, and assigned to the diffraction of (110), (200), (220) and (311) planes of cubic $Cu^{(I)}_2O$ nanoparticles with a mean crystallite size of 65 nm (JCPDS Card 00-005-0667). By contrast, in the case of $Cu(NO_3)_2$ precursor, additional diffraction peaks have been observed at 2θ = 38.8°, 54.0° and 58.0°, and assigned to the diffraction of (111), (020) and (202) planes of monoclinic $Cu^{(II)}O$ nanoparticles with a mean crystallite size of 10 nm (JCPDS Card 01-089-5895). Very interestingly, the choice of the photoassisted synthesis/deposition parameters allowed to selectively drive the oxidation state of the Cu nanoparticles synthesized on the ZnO support towards either cuprous or cupric oxides, so that the prepared catalysts could be considered as $Cu^{(I)}_2O$-ZnO or $Cu^{(II)}O$-ZnO. This suggests the possibility of controlling the oxidation state of the Cu nanoparticles in the Cu-ZnO while implementing a preparation procedure at room temperature without applying any final thermal treatment. Further complementary works are actually being performed for shedding light on this very interesting behavior, and therefore for highlighting the main synthesis parameters enabling to drive the oxidation state of the Cu within the Cu-ZnO material.

We have to note that performing the photodeposition process on the ZnO support led to an increase in the mean crystallite site of the semi-conductor host from 10 nm to 20 nm in the case of the copper nitrate precursor. By contrast, no significant change was observed in the case of the acetylacetonate precursor, with a mean crystallite size of 13 nm being obtained.

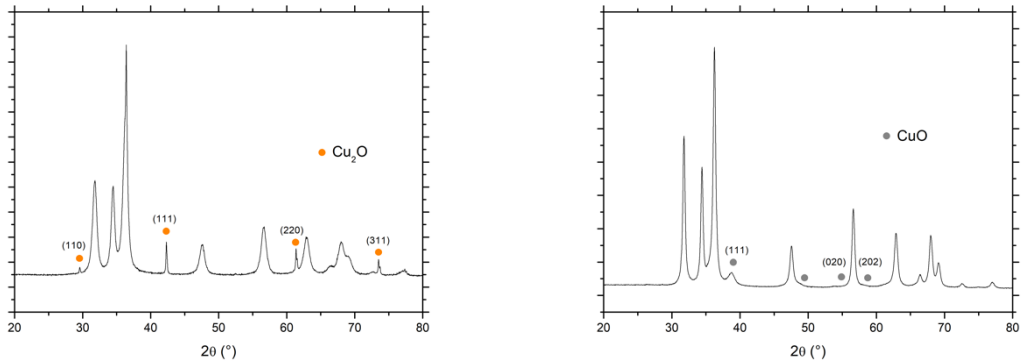

Figure 10. XRD pattern of the Cu/ZnO materials synthesized by photodeposition using (a) $Cu(acac)_2$ and (b) $Cu(NO_3)_2$ as metallic precursor.

Figure 11 shows the TEM images of the Cu-ZnO materials obtained by the photon-assisted synthesis method with both copper precursors. Unfortunatly, the similarities of the interplanar spacings corresponding to the main planes of the ZnO material and of both $Cu^{(II)}O$ and $Cu_2{}^{(I)}O$ crystallites did not allow to identify and locate specifically the different phases within the Cu-ZnO materials that consisted in very entangled oxide crystallites in close contact. Indeed, the (101) and (002) planes of ZnO have interplanar distances of 0.25 nm and 0.26 nm [JCPDS No.00-036-1451], while the (111) and (110) planes of the $Cu^{(II)}O$ phase have 0.23 nm and 0.27 nm interplanar distance respectively [JCPDS No. 01-089-5895] [37], and the (111) planes of the $Cu_2{}^{(I)}O$ crystallites have an interplanar distance of 0.25 [JCPDS No. 00-005-0667] [38].

It is worth noting that whatever the copper precursor, the prepared material can be considered as a Cu-ZnO composite catalyst since both Cu_2O and CuO crystallites do not exhibit significantly smaller mean sizes than the ZnO crystallites, rather than as a ZnO supported Cu catalyst, that would usually consist in smaller size Cu-based nanoparticles dispersed on the ZnO support. Considering the exclusive presence of one single chemical state for the crystalline Cu-based crystallites in the samples as shown by XRD - keeping in mind the detection limit of the XRD measurement -, the Cu-ZnO materials can thus be considered as $Cu^{(II)}O$-ZnO and $Cu_2{}^{(I)}O$-ZnO composite catalysts, although the assignment of both transition metal oxide phases to specific crystallites in TEM images was not possible.

Peer-reviewed version available at Materials 2018, 11, 2260; doi:10.3390/ma11112260

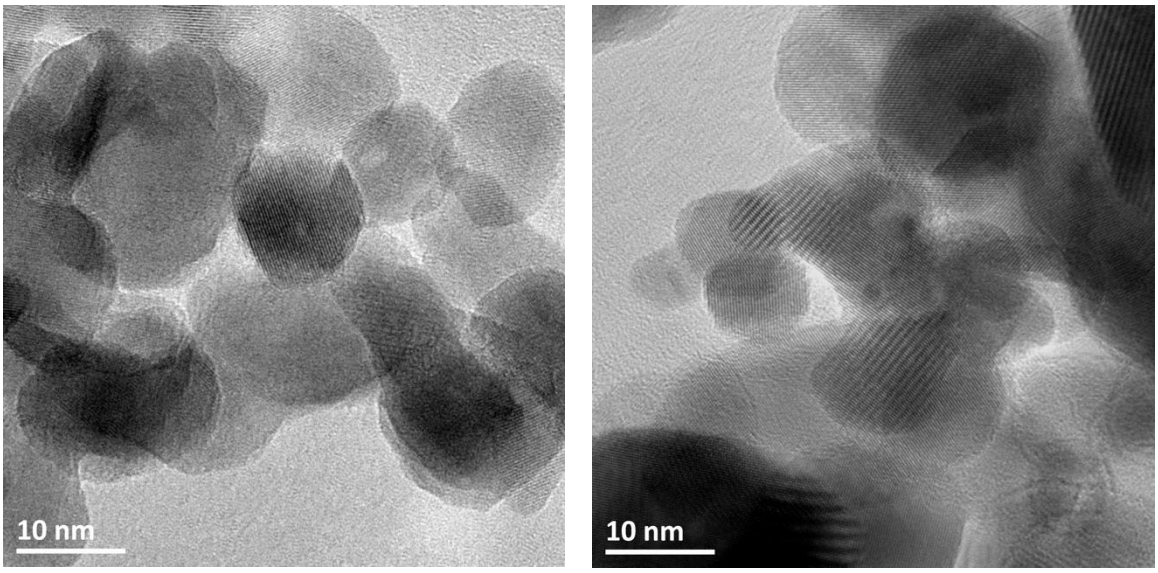

(**a**) (**b**)

Figure 11. TEM images of the Cu-ZnO materials synthesized by photodeposition using (a) $Cu(acac)_2$ and (b) $Cu(NO_3)_2$ as metallic precursor.

5. Conclusions

Cu_xO-ZnO composite catalysts with a control of the chemical state of the copper oxide phase have been prepared at room temperature using the solar light-induced redox photoactivity of the ZnO semiconductor support. The preparation of $Cu_2^{(I)}O$-ZnO and $Cu^{(II)}O$-ZnO composite catalysts was achieved by using $Cu(acac)_2$ in THF-water and $Cu(NO_3)_2$ in water as metallic precursor, respectively. The photoactive ZnO host material was prepared through the precipitation method with carbonate as precipitation agent, and its superior activity compared to other ZnO materials synthesized by other methods was evaluated by taking the photocatalytic degradation of the 4-chlorophenol compound in water under simulated solar light as model reaction.

Works are ongoing for understanding the key-parameters driving the selective synthesis of the Cu_xO phase within the ZnO-based catalysts. The activity of Cu_xO-ZnO catalysts will be investigated in reactions of high applicative interest within the biomass conversion process. Beside thermal catalysis applications, this work opened a new route for the facile synthesis of Cu_2O-ZnO heterojunction photocatalysts, that could take advantage under solar light of the heterojunction built between the *p*-type semi-conductor Cu_2O with direct band gap of about 2.17 eV and the ZnO semiconductor phase.

Author Contributions: Experimental works, M.B. and P.G.M.; Data analysis, M.B., P.G.M., A.R. and N.K.; Writing-Original Draft Preparation, P.G.M. and N.K.; Visualization, P.G.M. and M.B.; Supervision, N.K. and A.R.; Project Administration, N.K.; Funding Acquisition, M.B., N.K. and A.R.

Funding: The authors gratefully acknowledge that this work was financially supported by a grant from the National Center of Science (NCN) in Krakow (Poland) (2016/22/E/ST4/00550). This research was co-funded by the Erasmus+ program of the European Union.

Acknowledgments: T. Dintzer (ICPEES, Strasbourg) and D. Ihiawakrim (IPCMS, Strasbourg) are acknowledged for performing SEM and TEM characterization, respectively.

Conflicts of Interest: The authors declare no conflict of interest.

References

1. Kołodziejczak-Radzimska, A.; Jesionowski, T. Zinc Oxide From Synthesis to Application: A Review. *Materials* **2014**, *7*, DOI doi: 10.3390/ma7042833.

2. Segets, D.; Gradl, J.; Taylor, R.K.; Vassilev, V.; Peukert, W. Analysis of Optical Absorbance Spectra for the Determination of ZnO Nanoparticle Size Distribution, Solubility, and Surface Energy. *ACS Nano* **2009**, *3*, 1703-1710, DOI doi: 10.1021/nn900223b.

3. Chaari, M.; Matoussi, A. Electrical conduction and dielectric studies of ZnO pellets. *Physica B: Condensed Matter* **2012**, *407*, 3441-3447, DOI https://doi.org/10.1016/j.physb.2012.04.056.

4. Bacaksiz, E.; Parlak, M.; Tomakin, M.; Özçelik, A.; Karakız, M.; Altunbaş, M. The effects of zinc nitrate, zinc acetate and zinc chloride precursors on investigation of structural and optical properties of ZnO thin films. *Journal of Alloys and Compounds* **2008**, *466*, 447-450, DOI https://doi.org/10.1016/j.jallcom.2007.11.061.

5. Wang, Z.L. Splendid One-Dimensional Nanostructures of Zinc Oxide: A New Nanomaterial Family for Nanotechnology. *ACS Nano* **2008**, *2*, 1987-1992, DOI: 10.1021/nn800631r

6. Wang, J.; Cao, J.; Fang, B.; Lu, P.; Deng, S.; Wang, H. Synthesis and characterization of multipod, flower-like, and shuttle-like ZnO frameworks in ionic liquids. *Mater Lett* **2005**, *59*, 1405-1408, DOI https://doi.org/10.1017/S1431927606060430

7. Sudha, D.; Sivakumar, P. Review on the photocatalytic activity of various composite catalysts. *Chemical Engineering and Processing: Process Intensification* **2015**, *97*, 112-133, DOI https://doi.org/10.1016/j.cep.2015.08.006.

8. Anderson Janotti and Chris G Van,de Walle Fundamentals of zinc oxide as a semiconductor. *Reports on Progress in Physics* **2009**, *72*, 126501, DOI https://doi.org/10.1088/0034-4885/72/12/126501

9. Reynolds, D.C.; Look, D.C.; Jogai, B.; Litton, C.W.; Cantwell, G.; Harsch, W.C. Valence-band ordering in ZnO. *Phys Rev B* **1999**, *60*, 2340-2344 DOI https://doi.org/10.1103/PhysRevB.60.2340

10. Chen, Y.; Bagnall, D.M.; Koh, H.; Park, K.; Hiraga, K.; Zhu, Z.; Yao, T. Plasma assisted molecular beam epitaxy of ZnO on c -plane sapphire: Growth and characterization. *J Appl Phys* **1998**, *84*, 3912-3918, DOI https://doi.org/10.1063/1.368595

11. Udom, I.; Ram, M.K.; Stefanakos, E.K.; Hepp, A.F.; Goswami, D.Y. One dimensional-ZnO nanostructures: Synthesis, properties and environmental applications. *Materials Science in Semiconductor Processing* **2013**, *16*, 2070-2083, DOI https://doi.org/10.1016/j.mssp.2013.06.017.

12. Hernández-Carrillo, M.A.; Torres-Ricárdez, R.; García-Mendoza, M.F.; Ramírez-Morales, E.; Rojas-Blanco, L.; Díaz-Flores, L.L.; Sepúlveda-Palacios, G.E.; Paraguay-Delgado, F.; Pérez-Hernández, G. Eu-modified ZnO nanoparticles for applications in photocatalysis. *Catalysis Today* **2018**, DOI https://doi.org/10.1016/j.cattod.2018.04.060.

13. Machín, A.; Cotto, M.; Duconge, J.; Arango, J.C.; Morant, C.; Pinilla, S.; Soto-Vázquez, L.; Resto, E.; Márquez, F. Hydrogen production via water splitting using different Au@ZnO catalysts under UV–vis irradiation. *Journal of Photochemistry and Photobiology A: Chemistry* **2018**, *353*, 385-394, DOI https://doi.org/10.1016/j.jphotochem.2017.11.050.

14. Fkiri, A.; Santacruz, M.R.; Mezni, A.; Smiri, L.-; Keller, V.; Keller, N. One-pot synthesis of lightly doped $Zn_{1-x}Cu_xO$ and Au–$Zn_{1-x}Cu_xO$ with solar light photocatalytic activity in liquid phase. *Environ Sci Pollut Res* **2017**, *24*, 15622-15633 DOI https://doi.org/10.1007/s11356-017-9067-5

15. Liu, Y.; Zhong, M.; Shan, G.; Li, Y.; Huang, B.; Yang, G. Biocompatible ZnO/Au Nanocomposites for Ultrasensitive DNA Detection Using Resonance Raman Scattering. *J Phys Chem B* **2008**, *112*, 6484-6489 DOI: 10.1021/jp710399d

16. Udawatte, N.; Lee, M.; Kim, J.; Lee, D. Well-Defined Au/ZnO Nanoparticle Composites Exhibiting Enhanced Photocatalytic Activities. *ACS Appl Mater Interfaces* **2011**, *3*, 4531-4538 DOI: 10.1021/am201221x

17. Li, H.; Liu, E.; Chan, F.Y.F.; Lu, Z.; Chen, R. Fabrication of ordered flower-like ZnO nanostructures by a microwave and ultrasonic combined technique and their enhanced photocatalytic activity. *Materials Letters* **2011**, *65*, 3440-3443, DOI https://doi.org/10.1016/j.matlet.2011.07.049.

18. Li, P.; Wei, Z.; Wu, T.; Peng, Q.; Li, Y. Auâ˜ZnO Hybrid Nanopyramids and Their Photocatalytic Properties. *J Am Chem Soc* **2011**, *133*, 5660-5663, DOI: 10.1021/ja111102u

19. Chen, P.; Lee, G.; Anandan, S.; Wu, J.J. Synthesis of ZnO and Au tethered ZnO pyramid-like microflower for photocatalytic degradation of orange II. *Materials Science and Engineering: B* **2012**, *177*, 190-196, DOI https://doi.org/10.1016/j.mseb.2011.12.001.

20. Sun, Q.; Men, Y.; Wang, J.; Chai, S.; Song, Q. Support effect of Ag/ZnO catalysts for partial oxidation of methanol. *Inorganic Chemistry Communications* **2018**, *92*, 51-54, DOI https://doi.org/10.1016/j.inoche.2018.04.001.

21. Grunwaldt, J.-.; Molenbroek, A.M.; Topsøe, N.-.; Topsøe, H.; Clausen, B.S. In Situ Investigations of Structural Changes in Cu/ZnO Catalysts. *Journal of Catalysis* **2000**, *194*, 452-460, DOI https://doi.org/10.1006/jcat.2000.2930.

22. Ichikawa, M. Catalysis by Supported Metal Crystallites from Carbonyl Clusters. I. Catalytic Methanol Synthesis under Mild Conditions over Supported Rhodium, Platinum, and Iridium Crystallites Prepared from Rh, Pt, and Ir Carbonyl Cluster Compounds Deposited on ZnO and MgO. *Bull Chem Soc Jpn* **1978**, *51*, 2268-2272, DOI https://doi.org/10.1246/bcsj.51.2268

23. Cubeiro, M.L.; Fierro, J.L.G. Selective Production of Hydrogen by Partial Oxidation of Methanol over ZnO-Supported Palladium Catalysts. *Journal of Catalysis* **1998**, *179*, 150-162, DOI https://doi.org/10.1006/jcat.1998.2184.

24. Zheng, L.; Li, X.; Du, W.; Shi, D.; Ning, W.; Lu, X.; Hou, Z. Metal-organic framework derived Cu/ZnO catalysts for continuous hydrogenolysis of glycerol. *Applied Catalysis B: Environmental* **2017**, *203*, 146-153, DOI https://doi.org/10.1016/j.apcatb.2016.10.011.

25. Alba-Rubio, A.C.; Santamaría-González, J.; Mérida-Robles, J.M.; Moreno-Tost, R.; Martín-Alonso, D.; Jiménez-López, A.; Maireles-Torres, P. Heterogeneous transesterification processes by using CaO supported on zinc oxide as basic catalysts. *Catalysis Today* **2010**, *149*, 281-287, DOI https://doi.org/10.1016/j.cattod.2009.06.024.

26. Zhu, Y.; Kong, X.; Zheng, H.; Ding, G.; Zhu, Y.; Li, Y. Efficient synthesis of 2,5-dihydroxymethylfuran and 2,5-dimethylfuran from 5-hydroxymethylfurfural using mineral-derived Cu catalysts as versatile catalysts. *Catal Sci Technol* **2015**, *5*, 4208-4217, DOI 10.1039/C5CY00700C

27. Llorca, J.; de la Piscina, P.R.; Dalmon, J.; Sales, J.; Homs, N. CO-free hydrogen from steam-reforming of bioethanol over ZnO-supported cobalt catalysts: Effect of the metallic precursor. *Applied Catalysis B: Environmental* **2003**, *43*, 355-369, DOI https://doi.org/10.1016/S0926-3373(02)00326-0.

28. Homs, N.; Llorca, J.; de la Piscina, P.R. Low-temperature steam-reforming of ethanol over ZnO-supported Ni and Cu catalysts: The effect of nickel and copper addition to ZnO-supported cobalt-based catalysts. *Catalysis Today* **2006**, *116*, 361-366, DOI https://doi.org/10.1016/j.cattod.2006.05.081.

29. Ammari, F.; Lamotte, J.; Touroude, R. An emergent catalytic material: Pt/ZnO catalyst for selective hydrogenation of crotonaldehyde. *Journal of Catalysis* **2004**, *221*, 32-42, DOI https://doi.org/10.1016/S0021-9517(03)00290-2.

30. Spencer, M.S. The role of zinc oxide in Cu/ZnO catalysts for methanol synthesis and the water gas shift reaction. *Topics in Catalysis* **1999**, *8*, 259, DOI: 10.1021/jp990375a

31. Pinna, F. Supported metal catalysts preparation. *Catalysis Today* **1998**, *41*, 129-137, DOI https://doi.org/10.1016/S0920-5861(98)00043-1.

32. Lee, K.M.; Lai, C.W.; Ngai, K.S.; Juan, J.C. Recent developments of zinc oxide based photocatalyst in water treatment technology: A review. *Water Research* **2016**, *88*, 428-448, DOI https://doi.org/10.1016/j.watres.2015.09.045.

33. Gaya, U.I.; Abdullah, A.H.; Zainal, Z.; Hussein, M.Z. Photocatalytic treatment of 4-chlorophenol in aqueous ZnO suspensions: Intermediates, influence of dosage and inorganic anions. *Journal of Hazardous Materials* **2009**, *168*, 57-63, DOI https://doi.org/10.1016/j.jhazmat.2009.01.130.

34. Eslami, A.; Hashemi, M.; Ghanbari, F. Degradation of 4-chlorophenol using catalyzed peroxymonosulfate with nano-MnO_2/UV irradiation: Toxicity assessment and evaluation for industrial wastewater treatment. *Journal of Cleaner Production* **2018**, *195*, 1389-1397, DOI https://doi.org/10.1016/j.jclepro.2018.05.137.

35. Ma, X.; Li, H.; Liu, T.; Du, S.; Qiang, Q.; Wang, Y.; Yin, S.; Sato, T. Comparison of photocatalytic reaction-induced selective corrosion with photocorrosion: Impact on morphology and stability of Ag-ZnO. *Applied Catalysis B: Environmental* **2017**, *201*, 348-358, DOI https://doi.org/10.1016/j.apcatb.2016.08.029.

36. Han, C.; Yang, M.; Weng, B.; Xu, Y. Improving the photocatalytic activity and anti-photocorrosion of semiconductor ZnO by coupling with versatile carbon. *Phys Chem Chem Phys* **2014**, *16*, 16891-16903, DOI 10.1039/C4CP02189D

37. Liu, Y.; Zhong, L.; Peng, Z.; Song, Y.; Chen, W. Field emission properties of one-dimensional single CuO nanoneedle by in situ microscopy. *J Mat Sci* **2010**, 45, 3791–3796, DOI https://doi.org/10.1007/s10853-010-4433-4

38. Kim, M.H.; Lim, B.; Lee, E.; Xia, Y. Polyol synthesis of Cu2O nanoparticles: use of chloride to promote the formation of a cubic morphology. *J Matter Chem* **2008**, 18, 4069-4073, DOI: 10.1039/b805913f